Journal Pre-proofs

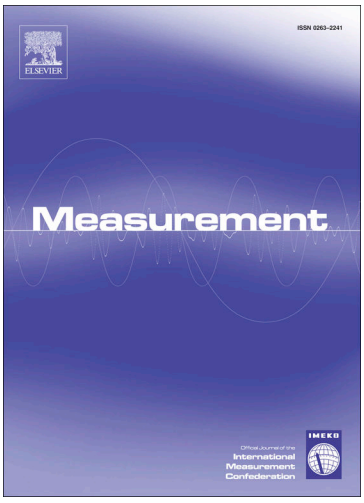

Weight Coefficient Calculation through Equivalent Ray Tracing Method for Light Field Particle Image Velocimetry

Xiaoyu Zhu, Moinul Hossain discussion, Jian Li, Biao Zhang, Chuanlong Xu

PII: S0263-2241(22)00255-X
DOI: https://doi.org/10.1016/j.measurement.2022.110982
Reference: MEASUR 110982

To appear in: *Measurement*

Received Date: 15 December 2021
Revised Date: 16 February 2022
Accepted Date: 4 March 2022

Please cite this article as: X. Zhu, M. Hossain discussion, J. Li, B. Zhang, C. Xu, Weight Coefficient Calculation through Equivalent Ray Tracing Method for Light Field Particle Image Velocimetry, *Measurement* (2022), doi: https://doi.org/10.1016/j.measurement.2022.110982

Weight Coefficient Calculation through Equivalent Ray Tracing Method for Light Field Particle Image Velocimetry

Xiaoyu Zhu[1], Md. Moinul Hossain[2], Jian Li[1,*], Biao Zhang[1], Chuanlong Xu[1,*]

[1] *National Engineering Research Center of Turbo-Generator Vibration, School of Energy and Environment, Southeast University, Nanjing 210096, China*

[2] *School of Engineering, University of Kent, Canterbury, Kent, CT2 7NT, UK*

[*] *Corresponding author: chuanlongxu@seu.edu.cn (C. Xu), eelijian@seu.edu.cn (J. Li)*

Abstract: Light field particle image velocimetry (LF-PIV) can measure three-dimensional (3D) flow velocity from a single snapshot of a light field camera based on the 3D reconstruction of tracer particles of light field images. However, it requires light field intensity calibrations to calculate accurate weight coefficients. Conventionally, the weight coefficients are calculated through in-situ calibration approaches whereas the translation of the calibration board within the entire measurement area is required. Therefore, these approaches are inapplicable for internal industrial flows and space-constrained applications. This study presents an equivalent ray tracing method for the weight coefficients calculation. With a light field snapshot of a smart calibration board, a mapping relationship is established to relate the target points sampled in the flow field with their equivalent points in the air. The weight coefficients are then calculated through the ray tracing method by changing the starting points of ray tracing from the target points to their equivalent points. The calculated weight coefficients are employed to reconstruct the feature marks of the calibration board. Results show that the spatial locations of the marks can be reconstructed accurately with a mean lateral and depth error of 0.63% and 5.6%, respectively. Experiments were also carried out on a low-speed laminar flow. The result indicates that the equivalent ray tracing method provides a similar measurement accuracy with the in-situ calibration method. The overall error of 6.77% is achieved for the velocity measurement. It is demonstrated that the proposed method is capable of measuring the 3D flow velocity for internal industrial and space-constrained applications without translating the calibration board within the entire measurement area.

Keywords: Flow measurement, Light field PIV, Weight coefficient, Equivalent point, Ray tracing

1. Introduction

In nature, most of the industrial flows are three-dimensional (3D), complex and turbulent. They likely contain a large range of length scales and a large dynamic range. For an in-depth understanding of complex flow structures and hence the design of relevant facilities of the industrial flows, it is crucial to develop an advanced flow diagnostic technique that can measure the instantaneous 3D velocity field. The particle image velocimetry (PIV) and its development show a capability of measuring the 3D velocity field [1–5]. However, most of the volumetric PIV techniques such as the tomographic PIV [6] and synthetic aperture PIV [7] are based on multiple cameras and require multiple optical access to the measurement area, thus limiting the applicability of internal industrial flows. Therefore, it is necessary to explore a single-perspective-based flow measurement technique for space-constraint applications.

Recently, the 3D-PIV techniques have been developed based on a single light field (LF) camera [8–12]. With the integration of a high-resolution microlens array (MLA) in front of the photosensor, the 3D spatial information of the tracer particles can be captured from a single perspective [13,14]. To retrieve the particle distributions from the LF images for 3D particle motion analysis, the measurement area is discretized as a 3D array of cubic voxels and tomographic algorithms are then used to perform the volumetric reconstruction [15–17]. The weight coefficient, which characterizes the intensity contribution of each discrete voxel to the LF image, requires to be determined for the particle reconstruction. Theoretically, with the geometrical location of the measurement area and optical parameters of the LF camera, the weight coefficient can be calculated through a direct ray tracing method [18], i.e., tracing the light rays from the target voxel to the image sensor. However, in practical experiments, the ray tracing from the target voxels is hampered by the light ray deflections in the object space, which is caused by the refractive index changes [19,20]. Considering that the light ray from the tracer particles passes through the flow, optical window and air, refractions must exist at the interfaces. Unfortunately, in experiments, the exact distances from the interfaces to the principal plane of the camera lens can hardly be measured, hence unable to trace the light rays from the flow field. Several in-situ calibration methods have been developed to resolve this issue. For instance, Wieneke et al. [21] proposed a volumetric self-calibration (VSC) method to correct the mapping functions between the voxels and pixels. It employs triangulation to lock the 3D positions of the particles and uses the residual triangulation error for corrections. The VSC method is further enhanced with the ghost particle suppression technique [22], which becomes the standard calibration procedure in stereo and tomographic PIV [23–26]. Besides, Hall et al. [27] developed a direct volumetric calibration (DLFC) approach to relate the world coordinates with the MLA coordinates through a polynomial mapping function without prior knowledge of the optical parameters. Recently, Shi et al. [28] proposed an enhanced volumetric calibration technique to relate the voxels with their affect pixels directly. This method exploits the unique point-like features of LF images to derive an object-image mapping function and the Monte Carlo method is combined to generate the weight coefficients.

These volumetric calibration approaches correct the ray tracing misalignments in the multi-media photogrammetry effectively and thus generate accurate weight coefficients for the LF-PIV. However, under some special circumstances, limitations still exist. For example, a crucial step of these approaches is to image a calibration target at different depths of the measurement area, which is easy to implement in the laboratory but difficult in the industry internal flows where the motion

of the calibration target is limited. Besides, the mapping function obtained from the calibration process is only applicable to a specific depth range that the calibration target has traversed, which is relatively limited. Employment of the calibration result to the voxels outside this depth range creates significant errors. To overcome these limitations, it is desirable to develop an appropriate and accessible method for weight coefficients calculation, especially for space-constraint applications.

The LF camera shows a capability to record the spatial and directional information of the light rays, however, it is difficult to identify the starting points of the rays. It means that if two light rays start from the different optical media and strike the same point on the main lens with the same angle of incidence, the LF camera cannot tell where the rays come from. From this perspective, if the starting points of the light ray can be moved from the measurement area to the air, the weight coefficients can then be calculated through the ray tracing technique without prior knowledge of the flow interface locations.

To facilitate an accurate flow measurement in space-constrained applications, an equivalent ray tracing method is proposed in this study for the weight coefficients calculation. The proposed approach can generate the weight coefficients for tracer particle reconstruction through a single snapshot of the calibration board instead of moving the calibration board within the entire measurement area. The methodology of weight coefficient calculation is described. The accuracy of the calculated weight coefficients is evaluated by reconstructing the calibration board immersed in the water using both synthetic and experimental data. Experiments on a low-speed laminar flow are also conducted to validate the feasibility of the proposed method.

2. Equivalent ray tracing method

2.1 Ray tracing method

Compared with the conventional camera, the LF camera records complete 4D LF information (i.e., both the spatial and directional information of the light rays). This is due to the addition of a dense microlens array (MLA) in front of the photosensor. As shown in Fig. 1, the light rays emitting from the object point are firstly captured by the main lens and then focused on the MLA. The spatial information of the rays is hence registered on the microlens. Each microlens further redirects the incoming rays to different pixels on the photosensor based on their directions. The directional information of the rays can then be recorded by the individual pixel.

To retrieve the 3D spatial location of the object, the ray propagation process from the object space to the photosensor requires to be characterized. As demonstrated by Georgiev et al [29], the LF can be represented as a 4D plenoptic function $L(x, y, \theta, \varphi)$. As illustrated in Fig. 2, (x, y) and (θ, φ) define the intersection of the ray with a plane perpendicular to the optical axis and the propagation direction of the ray, respectively. Specifically, θ is the angle between the optical axis (z) and the projection of the ray on the x-z plane, and φ is the angle between the optical axis (z) and the projection of the ray on the y-z plane. The propagation trajectory of the light ray can be traced using the ray transfer matrix defined as

$$\begin{pmatrix} x' \\ y' \\ \theta' \\ \phi' \end{pmatrix} = \underbrace{\begin{bmatrix} 1 & 0 & s_\mu & 0 \\ 0 & 1 & 0 & s_\mu \\ 0 & 0 & 1 & 0 \\ 0 & 0 & 0 & 1 \end{bmatrix}}_{\text{MLA to photosensor}} \left(\underbrace{\begin{bmatrix} 1 & 0 & 0 & 0 \\ 0 & 1 & 0 & 0 \\ -1/f_m & 0 & 1 & 0 \\ 0 & -1/f_m & 0 & 1 \end{bmatrix}}_{\text{Through MLA}} + \begin{pmatrix} 0 \\ 0 \\ s_{ux}/f_m \\ s_{vy}/f_m \end{pmatrix} \right) \underbrace{\begin{bmatrix} 1 & 0 & s_i & 0 \\ 0 & 1 & 0 & s_i \\ 0 & 0 & 1 & 0 \\ 0 & 0 & 0 & 1 \end{bmatrix}}_{\text{Main lens to MLA}} \underbrace{\begin{bmatrix} 1 & 0 & 0 & 0 \\ 0 & 1 & 0 & 0 \\ -1/F_{\mathrm{m}} & 0 & 1 & 0 \\ 0 & -1/F_{\mathrm{m}} & 0 & 1 \end{bmatrix}}_{\text{Through main lens}} \underbrace{\begin{bmatrix} 1 & 0 & s_o & 0 \\ 0 & 1 & 0 & s_o \\ 0 & 0 & 1 & 0 \\ 0 & 0 & 0 & 1 \end{bmatrix}}_{\text{Object to main lens}} \begin{pmatrix} x \\ y \\ \theta \\ \phi \end{pmatrix} \quad (1)$$

where (x, y, θ, φ) and $(x', y', \theta', \varphi')$ are the 4D coordinates of the light ray starting from the object space and reaching the photosensor, respectively. s_o and s_i are the object and image distances, F_m and f_m are the focal lengths of the main lens and microlens, s_{ux} and s_{vy} are the distances from the microlens center to the optical axis in the x and y directions. s_μ is the distance from the MLA to the photosensor. Careful consideration should be taken to the object distance s_o as it is defined under a case that the light ray propagates along a straight path in the object space. Any ray deflections caused by the refractions requires additional modification of s_o, otherwise, misalignment of the ray tracing can be produced.

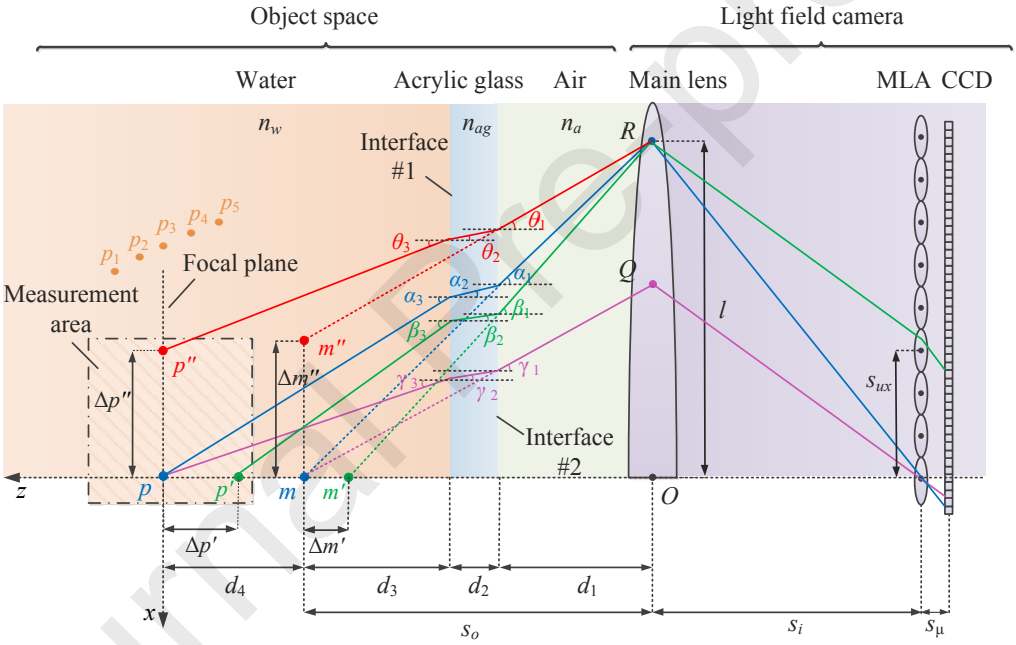

Fig. 1 Light ray propagations of the LF imaging in multiple optical media. p is the nominal focal point of the LF camera and m is p's equivalent point in the air. p' and p'' are the depth defocus point and lateral off-axis point, respectively, and m' and m'' are their equivalent points.

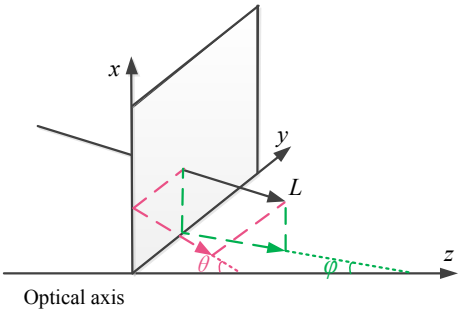

Fig. 2 Parameterization of the LF with a 4D plenoptic function $L(x, y, \theta, \varphi)$.

2.2 Determination of equivalent point

In the LF-PIV, the refraction indices should be employed carefully in the ray tracing method. Because the refractive index in the object space may change during the experiments. For example, in the air, if the liquid flow field is captured by the LF camera, the difference of refractive index between the liquid and air causes ray refractions. The optical window made by glass or acrylic glass can also cause ray deflections, which significantly degrades the ray tracing accuracy.

As illustrated in Fig. 1, point p is the nominal focal point of the LF camera, which is conjugated with the intersection of the MLA and the optical axis (z-axis). A light ray (blue solid line) emitting from p passes through the interfaces #1 and #2 with twice refractions, and finally intersects the main lens at point R. The position of R and the angle of incidence should be determined for further tracing the ray from the main lens to the photosensor. However, this demands the exact distances from the interfaces to the principal plane of the main lens, which is not feasible to measure in practical experiments. Fortunately, the LF camera cannot identify the propagation trajectories of the light rays in the object space. The rays start from different optical media and strike the same point of the main lens with a fixed angle of incidence will always light the same pixel on the photosensor. From this perspective, the ray trajectory from point p to R can be replaced by another ray starts from the air and propagates along the straight path. The starting point of the ray in the air (marked as m in Fig. 1) can be determined as the intersection of the ray extension (blue dot line) and the optical axis.

If the distance from interface #2 to the main lens is d_1, the separation between two interfaces is d_2, the distance from point m to interface #1 is d_3, and the separation between m and p is d_4, based on the triangular transformation, the relationships would be

$$\left(d_1 + d_2 + d_3\right)\tan\alpha_1 = d_1\tan\alpha_1 + d_2\tan\alpha_2 + \left(d_3 + d_4\right)\tan\alpha_3 \tag{2}$$

where α_3 is the angle of incidence, and α_2 and α_1 are the angles of refraction. Eq. (2) can be simplified with the defined refractive indices of water n_w, acrylic glass n_{ag} and air n_a, as

$$d_1 + d_2 + d_3 = d_1 + d_2\left(n_a / n_{ag}\right) + \left(d_3 + d_4\right)\left(n_a / n_w\right) \tag{3}$$

The Snell's law,

$$n_a \sin\alpha_1 = n_{ag}\sin\alpha_2 = n_w \sin\alpha_3 \tag{4}$$

and the paraxial approximation is applied in derivation of Eq. (3).

$$\sin\alpha \approx \tan\alpha \approx \alpha \tag{5}$$

Equation (3) indicates that with the paraxial approximation, the distance from point m to the main lens (i.e., $d_1 + d_2 + d_3$) is independent of the angle of incidence. It means that if there is another ray that starts from point p and strikes the main lens at point Q (purple solid line in Fig. 1), the extension of the ray from Q will also intersect the optical axis at point m. Thus, it can be inferred that points p and m are equivalent, and the starting point of the ray can be moved from p to m for tracing the ray to the same pixel. In this aspect, the interface locations are not necessary and the problem becomes the localization of the equivalent point m. Since p is the nominal focal point in the water, its equivalent point in the air should also be the nominal focal point, whose location can be determined based on the thin lens model, as

$$d_1 + d_2 + d_3 = F_{\mathrm{m}}\left(M - 1\right)/M \tag{6}$$

where M denotes the magnification of the main lens. According to Eq. (6), with the known lens parameters, the ray transfer matrix [in Eq. (1)] can be used to trace the rays starting from m instead of p to the photosensor.

In addition to the focal point p, for a defocus point (p') with known defocus distance ($\Delta p'$) and an off-axis point (p'') with known off-axis distance ($\Delta p''$), their equivalent points (m' and m'') can be determined based on the geometrical optics. Specifically, the defocus distance of the point m' ($\Delta m'$ in Fig. 1) and off-axis distance of point m'' ($\Delta m''$ in Fig. 1) can be related to $\Delta p'$ and $\Delta p''$, respectively, based on the triangular transformation, as

$$\left(d_1+d_2+d_3-\Delta m'\right)\tan\beta_1 = d_1\tan\beta_1 + d_2\tan\beta_2 + \left(d_3+d_4-\Delta p'\right)\tan\beta_3 \tag{7}$$

$$\left(d_1+d_2+d_3\right)\tan\theta_1 + \Delta m'' = d_1\tan\theta_1 + d_2\tan\theta_2 + \left(d_3+\cdot d_4\right)\tan\theta_3 + \Delta p'' \tag{8}$$

By eliminating d_4 through Eq. (2) and employing the Snell's law and paraxial approximation, Eqs. (7) and (8) can be simplified as

$$\Delta m' = \left(n_a/n_w\right)\Delta p' \tag{9}$$

$$\Delta m'' = \Delta p'' \tag{10}$$

Eq. (9) indicates that the ratio of $\Delta m'$ to $\Delta p'$ is only dependent on the refractive indices of the flow field medium and the air, and it will not be affected by the optical window. As the location of point m is known, the object distance of m' can further be calculated with the defocus distance obtained from Eq. (9). Eq. (10) indicates that lateral off-axis distances will always be the same in the flow field and the air. The starting point of ray tracing can therefore be changed from point p'' to m'' by setting the lateral location coordinate in Eq. (1) as $x = \Delta p''$. The object distance of point m'' is the same as point m. For a point with both lateral off-axis distance and depth defocus distance, its equivalent point can also be determined by Eqs. (6), (9) and (10). Therefore, the rays from the equivalent point can be traced to the photosensor through the ray transfer matrix [in Eq. (1)].

2.3 Weight coefficient calculation

To reconstruct the volume of tracer particles from a LF image, the measurement area can be discretized as a 3D array of cubic voxel elements in the x, y, and z-directions. The projection of light intensity distribution $E(x, y, z)$ on an image pixel returns the pixel's intensity $I(x, y)$, which can be expressed as a linear equation

$$\sum_{j\in N} w_{i,j} E\left(x_j, y_j, z_j\right) = I\left(x_i, y_i\right) \tag{11}$$

where $w_{i,j}$ is the weight coefficient that describes the light intensity contribution of the j_{th} voxel to the i_{th} pixel, and N denotes the number of the voxels in the line-of-the-sight of the i_{th} pixel. With the captured light field images and the calculated weight coefficients, the goal of the particle reconstruction is to inversely solve this linear equation and determine the intensity distribution $E(x, y, z)$. As the number of particle projections is limited, there is an infinite number of solutions satisfying the Eq. (11). Therefore, additional conditions, e.g., entropy maximization, is considered to enforce uniqueness. In this study, the simultaneous algebraic iterative technique (SART) [30] based on the maximum entropy criterion is employed. In the SART, the iteration starts with a uniform initial guess and the voxel intensity is updated iteratively via the following expression

$$E_j^{k+1} = E_j^k + \mu \frac{\sum_i \left(\frac{I_i - \sum_{n=1}^{N} w_{i,n} E_n^k}{\sum_{n=1}^{N} w_{i,n}} \right) w_{i,j}}{\sum_i w_{i,j}} \tag{12}$$

where E_j^k denotes the voxel intensity in k_{th} iteration, I_i denotes the pixel intensity, μ is the relaxation parameter. In this algorithm, the correct magnitude of voxel's intensity in each iteration depends on the difference between the actual pixel intensity and the product of the weight coefficient with the current voxel intensity. Therefore, the accuracy of the calculated weight coefficients has a significant effect on the final reconstruction accuracy.

To determine the light intensity contribution of the j_{th} voxel to the i_{th} pixel, the light beam emitting from the j_{th} voxel can be discretized as the dense light rays with different propagation directions, and the weight coefficient $w_{i,j}$ can be calculated as

$$w_{i,j} = N_{i,j} / N_j \tag{13}$$

where N_j denote the total number of the light rays that emit from the j_{th} voxel and are detected by the main lens, $N_{i,j}$ denotes the number of light rays that emit from the j_{th} voxel and strike the i_{th} pixel. Taking the red voxel in Fig. 3 as the j_{th} voxel, considering that a total of 10^4 light rays emitting from this voxel can be detected by the main aperture. Through the refractions of the main lens and the MLA, these rays converge on the 5×5 pixels (colored ones). These 5×5 pixels are the affected pixels of the j_{th} voxel [9]. Among them, the central pixel detects 1600 rays and thus the corresponding weight coefficient is 0.16. The sum of the weight coefficients of the affected pixels is equal to 1. In addition to the affected pixels, the other pixels on the photosensor are not lighted by the j_{th} voxel, and thus the corresponding weight coefficients are all equal to 0.

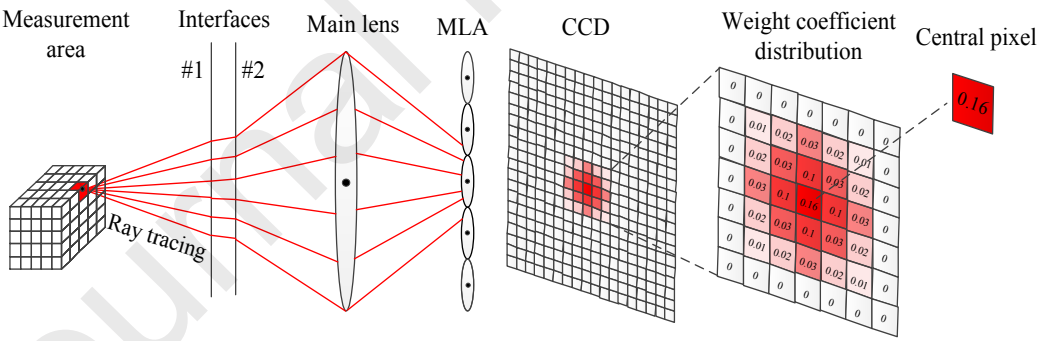

Fig. 3 An example of the weight coefficient calculation.

The number of rays that converge on each pixel can be counted by the equivalent ray tracing (ERT) method. Specifically, for a target voxel in the measurement area, several points within this voxel are sampled. Although these sampled points cannot be taken as the starting points of the ray tracing due to the unknown interface locations. Their equivalent points in the air can be determined by Eqs. (6), (9) and (10). It has been demonstrated (described in Section 2.2) that the starting points of the ray tracing can be moved from the target points to their equivalent points, and the ray tracing can be performed without the prior knowledge of the interface locations. With the densely sampled light rays from each equivalent point, the ray transfer matrix [Eq. (1)] is employed to trace the rays to the corresponding pixels. As a result, the number of rays that converge on each pixel (i.e., $N_{i,j}$)

and hence the weight coefficient can be calculated. In this study, to ensure the accuracy of the calculated weight coefficient, the measurement area is discretized as 0.1 mm×0.1 mm×0.1 mm cube voxels. The number of the points sampled in each voxel and the number of light rays sampled from each equivalent point are 500 and 10^4, respectively.

In the practical experiment, the location of the focal plane relative to the central depth of the measurement area must be determined to calculate the weight coefficients. This can be achieved by imaging a calibration target with feature marks (detailed in Section 4). As the measurement area is discretized into the voxels with uniform size, the determination of the focal plane can help to infer the defocus distances of the sampled point sources in each voxel, which are essential for the localization of the equivalent points by Eqs. (9) and (10). Fig. 4 illustrates the workflow of the ERT method for the weight coefficients calculation.

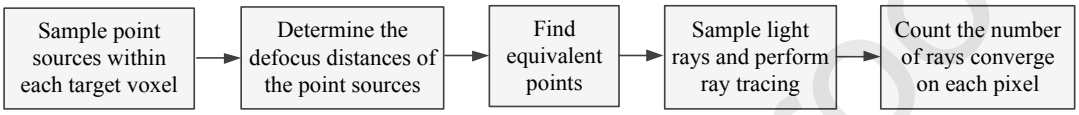

Fig. 4 Workflow of weight coefficient calculation through the equivalent ray tracing method.

3. Numerical simulation

3.1 Simulation setup

To verify the accuracy of the calculated weight coefficients, numerical simulations were carried out. As illustrated in Fig. 1, five discrete voxels p_1 to p_5 located in the measurement area are chosen to calculate their weight coefficients. The defocus distances of the voxel centers are given in Table 1. The refractive indices of air, acrylic glass and water are used as 1, 1.49 and 1.33, respectively. The distance from interface #2 to the main lens (d_1 in Fig. 1) is set as 98 mm, and the thickness of the acrylic glass (d_2) is set as 2 mm. The optical parameters of the LF camera are summarized in Table 2.

To calculate the weight coefficients of the voxels p_1 to p_5 by the ERT method, 500 point sources are randomly sampled at each target voxel. The equivalent points of these sampling points are then determined and 10^4 rays with different directions are traced from each equivalent point to the photosensor to compute the weight coefficient. On the other hand, as the distances from the interfaces to the main lens are given (i.e, d_1 and d_2), the weight coefficients can be calculated by directly tracing the rays starting from the target voxels (i.e., p_1 to p_5). By considering the refractions, the ray transfer matrix in the object space is modified as

$$\begin{pmatrix} x' \\ y' \\ \theta' \\ \phi' \end{pmatrix} = \underbrace{\begin{bmatrix} 1 & 0 & d_1 & 0 \\ 0 & 1 & 0 & d_1 \\ 0 & 0 & 1 & 0 \\ 0 & 0 & 0 & 1 \end{bmatrix}}_{\text{Interface 2 to main lens}} \underbrace{\begin{bmatrix} 1 & 0 & 0 & 0 \\ 0 & 1 & 0 & 0 \\ 0 & 0 & \frac{n_{ag}}{n_a} & 0 \\ 0 & 0 & 0 & \frac{n_{ag}}{n_a} \end{bmatrix}}_{\text{Refraction}} \underbrace{\begin{bmatrix} 1 & 0 & d_2 & 0 \\ 0 & 1 & 0 & d_2 \\ 0 & 0 & 1 & 0 \\ 0 & 0 & 0 & 1 \end{bmatrix}}_{\text{Interface 1 to 2}} \underbrace{\begin{bmatrix} 1 & 0 & 0 & 0 \\ 0 & 1 & 0 & 0 \\ 0 & 0 & \frac{n_w}{n_{ag}} & 0 \\ 0 & 0 & 0 & \frac{n_w}{n_{ag}} \end{bmatrix}}_{\text{Refraction}} \underbrace{\begin{bmatrix} 1 & 0 & d & 0 \\ 0 & 1 & 0 & d \\ 0 & 0 & 1 & 0 \\ 0 & 0 & 0 & 1 \end{bmatrix}}_{\text{Object to interface 1}} \begin{pmatrix} x \\ y \\ \theta \\ \phi \end{pmatrix} \tag{14}$$

In Eq. (14), d is the depth distance that the ray passes through the water, and can be calculated as

$$d = d_3 + d_4 + \Delta z \tag{15}$$

where d_3 and d_4 can be obtained from Eqs. (6) and (3), respectively, and Δz is the depth defocus

distance of the sampling point. By combining the modified ray transfer matrix [Eqs. (1) and (14)], densely sampled rays can be directly traced from the voxels p_1 to p_5 to the photosensor. The generated weight coefficients are then considered as the ground truth to evaluate the result of the ERT method.

Table 1: Defocus distances of centers of the target voxels p_1 to p_5 (mm)

	p_1	p_2	p_3	p_4	p_5
Lateral (x)	1	1.5	2	2.5	3
Lateral (y)	0	0	0	0	0
Depth (z)	4	2	0	-2	-4

Table 2: Optical parameters of the LF camera

Symbol	Parameter	Value	Unit
M	Magnification ratio	-1	-
F_m	Main lens focal length	100	mm
f_m	MLA focal length	0.8	mm
$(f/\#)_m$	Main lens f-number	4	-
$(f/\#)_{mla}$	MLA f-number	8	-
p_m	Main lens aperture	25	mm
p_l	Microlens pitch	0.1	mm
p_x	Pixel pitch	5.5	μm
s_i	Main lens to MLA distance	200	mm
s_μ	MLA to photosensor distance	0.8	mm
N_{px}	Camera resolution: x	2352	-
N_{py}	Camera resolution: y	1768	-
N_{mx}	MLA resolution: x	252	-
N_{my}	MLA resolution: y	252	-

3.2 Accuracy of the weight coefficient calculation

Fig. 5 shows a comparison of the weight coefficients calculated by the direct ray tracing (DRT) and ERT methods. A similar structure can be seen for both methods. As the depth defocus distance increases, the weight coefficient produces a larger point-like pattern on the image. These point-like features contain the depth information of the voxels that are used to reconstruct the tracer particle locations in the LF-PIV by the SART algorithm.

The weight coefficients calculated by the DRT and ERT methods are further quantified by the structural similarity index (SSIM) [31] and the root-mean-square error (RMSE). The SSIM index quantifies the similarity of two images and expressed as

$$\mathrm{SSIM}\left(w_1, w_2\right) = \frac{\left(2\mu_1\mu_2 + c_1\right)\left(2\sigma_{12} + c_2\right)}{\left(\mu_1^{\,2} + \mu_2^{\,2} + c_1\right)\left(\sigma_1^{\,2} + \sigma_2^{\,2} + c_2\right)} \tag{16}$$

where w_1 and w_2 denote the reference image and reconstructed image, respectively. μ_1, μ_2, σ_1, σ_2 and σ_{12} are the local means, standard deviations and cross-covariance for the reference image and reconstructed image. c_1 and c_2 are the regularization constants. The SSIM index is from 0 to 1, and a large value corresponds to a high similarity. The RMSE value is the standard deviation of the

residuals (in this work is the difference between the pixel gray value of two images). A small RMSE indicates that the difference between the two images is insignificant. As shown in Fig. 6, the SSIM value is approximately 1 and the RMSE is smaller than 2.5, indicating that the weight coefficients calculated by the ERT match well with the ground truth. The ERT method can hence be used to generate the weight coefficients in the case that the flow interface locations are not given.

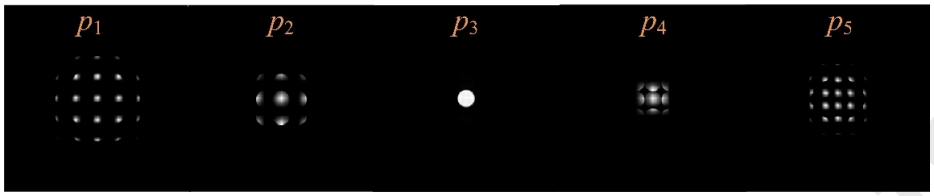

(a) DRT result

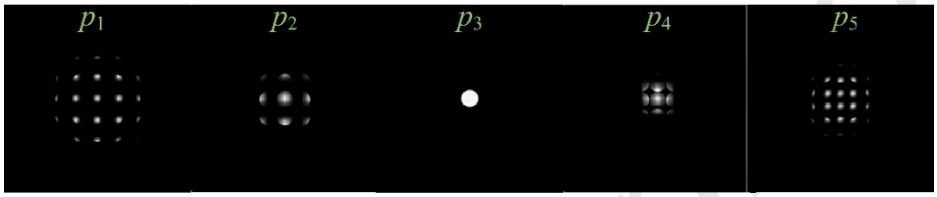

(b) ERT result

Fig. 5 Comparison of weight coefficients calculated by the DRT and ERT methods.

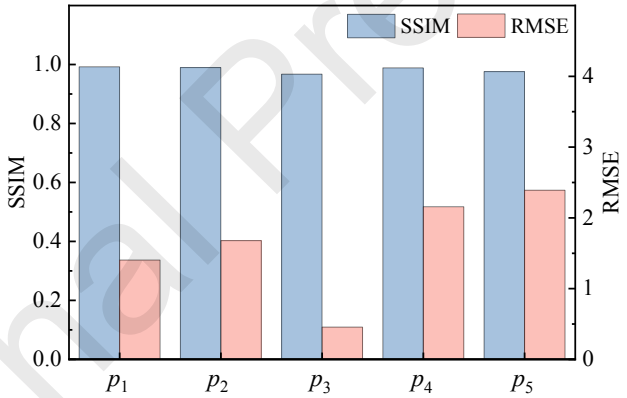

Fig. 6 SSIM index and RMSE of weight coefficients obtained by DRT and ERT methods.

3.3 Reconstruction of calibration board

The accuracy of the weight coefficients calculation is further verified by reconstructing a bespoke calibration board which is immersed in the water. The size of the calibration board is 8 mm ×8 mm and it contains a 7×7 dot pattern with a grid spacing of 1 mm. The diameter of each dot is 0.2 mm. As illustrated in Fig. 7, the x and y axes are perpendicular to the optical axis and correspond to the in-plane direction of the calibration board, while the z-axis is parallel to the optical axis and corresponds to the depth direction. The calibration board is translated along the depth direction in front and back of the focal plane (-8 mm < z < 8 mm, focal plane z = 0 mm) with a step-interval of 1 mm. The images of the calibration board at different depths are generated by the LF camera described in Section 3.1.

To reconstruct the calibration board at different depths, an 8 mm×8 mm×24 mm reconstructed volume is discretized into 80×80×240 voxels. The center of the reconstructed

volume is aligned with the nominal focal point in the water. In addition to the ERT method, the weight coefficients are also calculated by the volumetric calibration (DLFC) method presented by Hall et al. [27]. In the DLFC, a polynomial function that relates the ray's starting point location to the MLA location is established to calculate the weight coefficients. The weight coefficients calculated by the ERT and DLFC methods are considered in the SART algorithm to reconstruct the dot marks on the calibration board. To ensure the convergence of SART, 200 iterations are performed with a relaxation parameter of 1 [32].

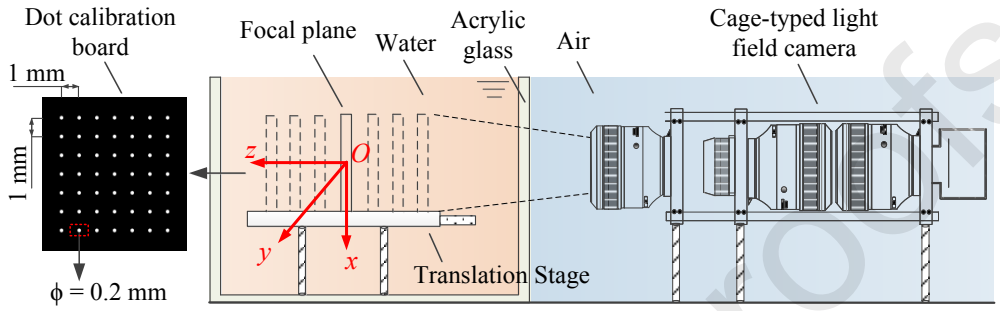

Fig. 7 Schematic of the translation of the dot calibration board along the depth direction in the water tank.

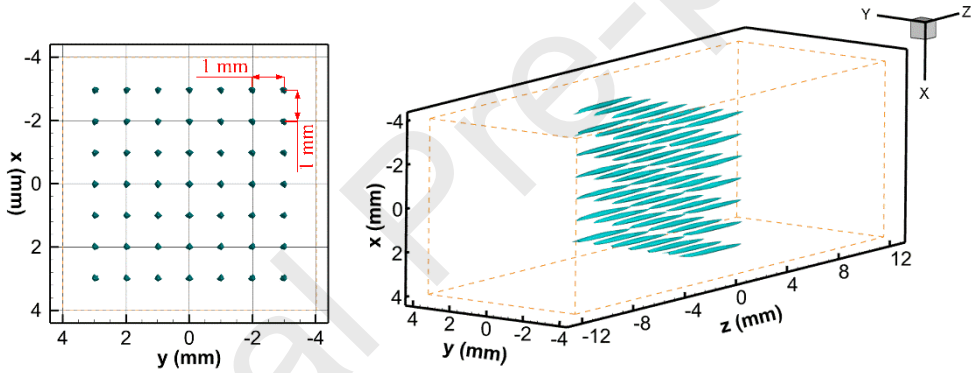

(a) *x*-*y* plot (b) 3D display

Fig. 8 Reconstructed dot structure of calibration board at $z = 0$ mm by ERT-SART.

Fig. 8 (a) illustrates the reconstructed calibration board at $z = 0$ mm by the ERT-SART method, where 7×7 dot array has been reconstructed accurately with a uniform lateral spacing of approximately 1 mm in the x and y-directions. Fig. 8 (b) shows the 3D presentation of the reconstructed dots. Noticeable elongation effects can be seen along the depth direction (z-axis). Such effects have also been observed in the tracer particle reconstruction of the LF-PIV [33,34] due to the limited viewing angle of the main lens (i.e., the angle between the outer edge of the main aperture and the optical axis [6]).

The mean and standard deviation of the reconstruction elongation length ($\overline{e_z}$ and σ) at different depths are calculated by Eqs. (17) and (18), respectively,

$$\overline{e_z} = \sum_{i=1}^{n} (e_z)_i \Big/ n \tag{17}$$

$$\sigma = \sqrt{\sum_{i=1}^{n} \left((e_z)_i - \overline{e_z}\right)^2 \Big/ n} \tag{18}$$

where n denotes the total number of dots on the calibration board, $(e_z)_i$ denotes the elongation length

of the i_{th} dot. The statistical result is compared with the DLFC-SART method, as illustrated in Fig. 9. It can be seen that the variations of $\overline{e_z}$ and σ obtained by DLFC-SART and ERT-SART are very similar. The depth elongation varies from 3.1 mm to 3.9 mm in the depth range of -8 mm < z < 8 mm and the standard deviation is smaller than 0.15 mm in this depth range. The mean elongation length at the focal plane (z = 0 mm) is shorter, but the corresponding standard deviation is larger than the other depths.

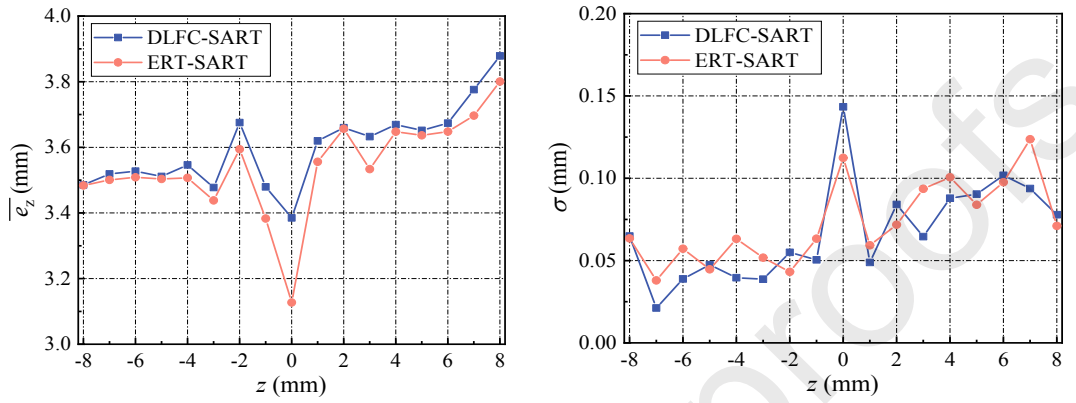

(a) Mean elongation $\overline{e_z}$ (b) Standard deviation σ

Fig. 9 Mean and standard deviation of reconstruction elongations under different depths obtained by DLFC-SART and ERT-SART methods.

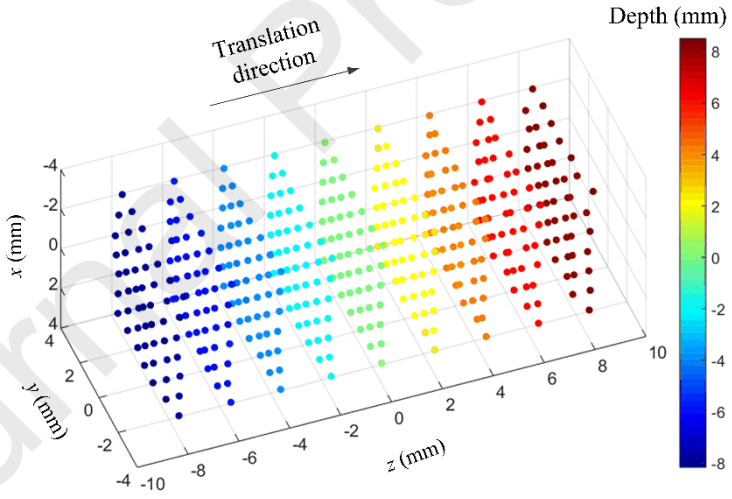

Fig. 10 Reconstructed dot centers at different depths obtained by the ERT-SART method.

To evaluate the accuracy of the reconstruction locations, the elongated dots are further extracted mainly for the center through the Gaussian peak fittings. Fig. 10 shows the extracted elongated dots from the ERT-SART reconstruction results, where the color map indicates the depth. It can be seen that the dots are reconstructed accurately under the different depths. The lateral and depth separations between the dots are also quantitatively evaluated. In the lateral direction, the x spacing of the 7×7 dot array in the same depth are averaged ($\overline{s_x}$) and compared with the exact grid spacing (x_g = 1 mm). The lateral reconstruction error (δ_x) can hence be determined as

$$\delta_x = \left|\overline{s_x} - x_g\right| / x_g \times 100\% \tag{19}$$

In the depth direction, the separations of 7×7 dots at adjacent depths are averaged ($\overline{s_z}$) and compared with the translation step-interval (z_s = 1 mm). The depth reconstruction error (δ_z) is calculated as

$$\delta_z = \left|\overline{s_z} - z_s\right| / z_s \times 100\% \tag{20}$$

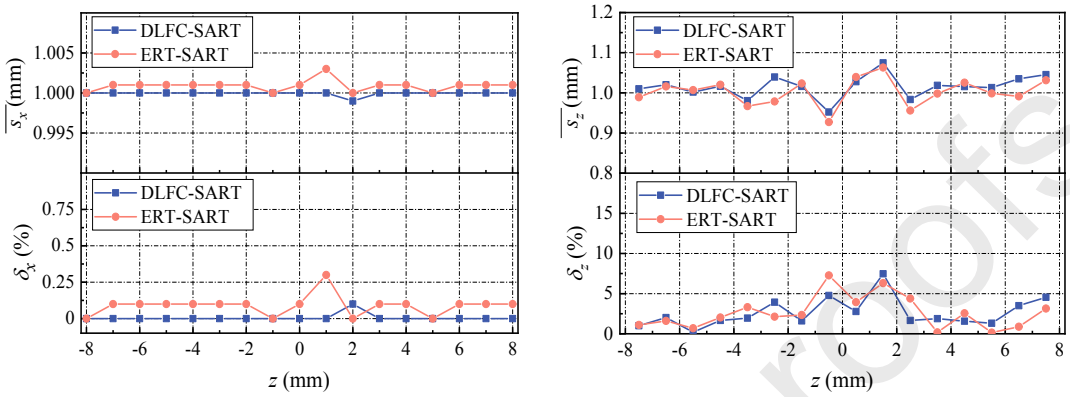

(a) Mean lateral spacing $\overline{s_x}$ and relative error δ_x (b) Mean depth distance $\overline{s_z}$ and relative error δ_z

Fig. 11 Variation of the reconstruction location error under different depths.

Figure 11 shows the error of location reconstruction obtained by the ERT-SART and DLFC-SART methods under different depths. It can be found that the lateral spacing is almost constant (i.e. ~1 mm) under different depths with a mean relative error of 0.09%, demonstrating a high reconstruction accuracy in the lateral direction. In contrast, the reconstruction accuracy degrades in the depth direction (z-axis). The depth spacing is from 0.92 mm to 1.08 mm with a mean relative error of 2.63%. This is mainly due to the lower resolution of the LF camera along the optical axis. To improve the depth resolution of the LF camera, enlarging the main aperture by adopting a lens with a large focal length and small *f*-number is an effective approach. Besides, adding a second LF camera to capture the object from another perspective can also mitigate the reconstruction elongation effect and reduce the reconstruction errors. Nevertheless, the result shown in Fig. 11 indicates that the ERT-SART method provides a similar reconstruction accuracy with the DLFC-SART method, demonstrating its feasibility for reconstructing the tracer particle using the LF-PIV technique.

4. Experimental results and discussions

4.1 Evaluation of reconstruction performance

Further to evaluate the reconstruction performance, reconstruction of a real calibration board immersed in the water is performed along with the lens distortions and noises. An 8 mm × 8 mm black calibration board with white dots painted is prepared. The pattern and grid spacing of the dot array are kept the same as the numerical calibration board. A high-resolution translation stage (Zolix APFP, resolution of 10 μm) is employed to translate the calibration board in the water, with similar depth ranges and step-intervals of the numerical test. To capture the images of the calibration board, a cage-typed LF camera (schematically shown in Fig. 7) is fabricated based on the optical parameters summarized in Table 2. The cage-typed LF camera consists of two head-to-head lenses

as a relay system and projects the image of the MLA to the photosensor at the ratio of 1:1. A detailed description of the camera can be found elsewhere in [17]. To compare the reconstruction results, the weight coefficients calculated by the DLFC and ERT methods are employed in the SART. An 8 mm×8 mm×24 mm volume with the voxel size of 0.1 mm×0.1 mm×0.1 mm is created. The center of the volume is aligned with the nominal focal point.

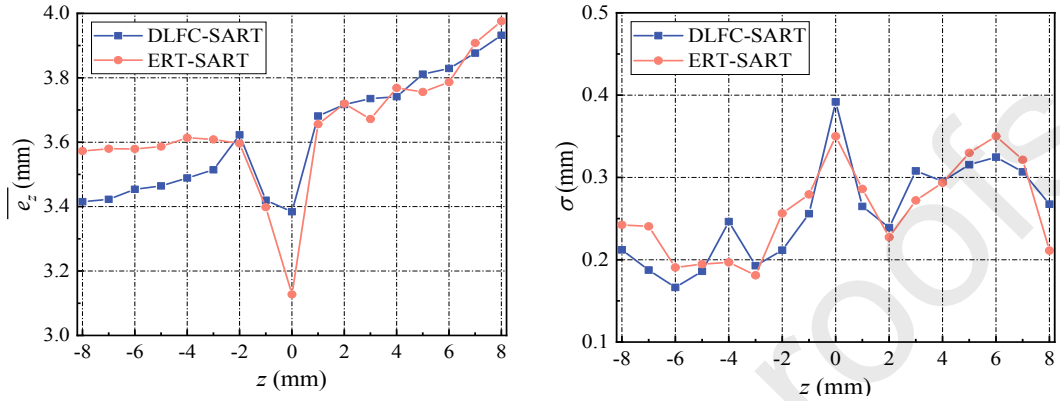

(a) Mean elongation $\bar{e}_z$ (b) Standard deviation σ

Fig. 12 Reconstructed elongations of the dots under different depths obtained by the ERT-SART and DLFC-SART.

Table 3: Average reconstruction elongation and location error in the range of -8 mm < z< 8 mm

	DLFC-SART		ERT-SART	
	Numerical	Experimental	Numerical	Experimental
Elongation length $\bar{e}_z$ (mm)	3.59	3.61	3.54	3.65
Standard deviation σ (mm)	0.07	0.25	0.08	0.27
Lateral location error δ_x (%)	0.03	0.11	0.09	0.63
Depth location error δ_z (%)	2.60	4.95	2.63	5.60

Figure 12 (a) illustrates the mean elongation lengths ($\bar{e}_z$) of the reconstructed dots under different depths, and Fig. 12 (b) illustrates the corresponding standard deviation (σ). It can be observed that $\bar{e}_z$ ranges from 3.1 mm to 4 mm, and σ is smaller than 0.4 mm. $\bar{e}_z$ and σ within the depth range of -8 mm < z < 8 mm is averaged and summarized in Table 3. It can been found that the elongation length is similar to the numerical result. The average elongation is around 3.6 mm. Besides, the standard deviation σ in the experiment is about 3.5 times larger than the numerical result, indicating that the elongation length at different depths is less uniform.

The reconstruction error of the dot locations under different depths (-8 mm < z < 8 mm) are illustrated in Fig. 13, and the averaged results in the entire depth range are listed in Table 3. It can be seen that both the lateral and depth location errors are larger than the numerical results (Table 3). This is mainly due to the lens distortions and assembly tolerances of the LF camera, which affect the ray tracing accuracy of the ERT method. Besides, it can be seen from Fig. 13 that the maximum errors of location reconstruction are found around the focal plane. It indicates that the depth resolution of the LF camera varies with the positions in the object space and it is significantly lower around the focal plane. This leads to the lower reconstruction accuracy.

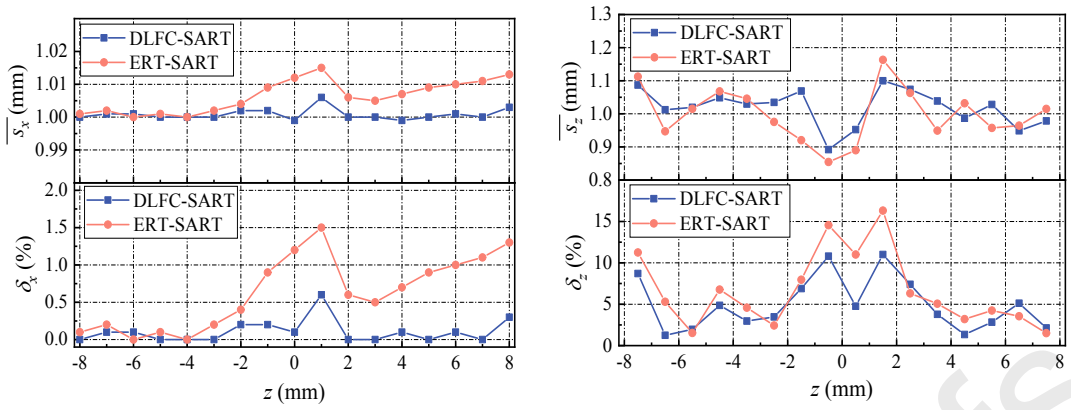

(a) Mean lateral spacing $\overline{s_x}$ and relative error δ_x (b) Mean depth distance $\overline{s_z}$ and relative error δ_z

Fig. 13 Experimental reconstruction location errors obtained by ERT-SART and DLFC-SART methods under different depths.

4.2 Experiments on a low-speed laminar flow

The uncertainty of velocity measurement of the ERT method is evaluated through experiments on a low-speed laminar flow. Fig. 14 shows the experimental setup of the laminar flow. The horizontal flow channel is made of 5 mm acrylic glass with a cross-section of 10×10 mm^2 (equivalent diameter D = 10 mm). The flow is generated by a metering pump and the flux is controlled via a PID regulator connected with an electric valve and an electromagnetic flowmeter. The flux is maintained at 40 L/h, yielding a constant mean velocity ($\bar{v}$) of 0.1082 m/s corresponding to the Reynolds number Re_D of 1100. The measurement area is set with spans of $D \times 1.3\ D \times D$ along the x, y and z-directions. A Nd:YAG double-pulsed laser (Beamtech, 200 mJ, 532 nm) with a beam expander is used to illuminate the measurement area. For PIV measurements, polyamide tracer particles with a mean diameter of 50 μm are homogenously seeded in the water, resulting in a particle concentration of 0.002 particles per pixel. The motion of the tracer particles is captured by the cage-typed LF camera with the optical settings listed in Table 2. The interval between two successive frames of the camera is set to 1.8 ms, yielding a maximum particle displacement of 0.4 mm corresponding to 4 voxels.

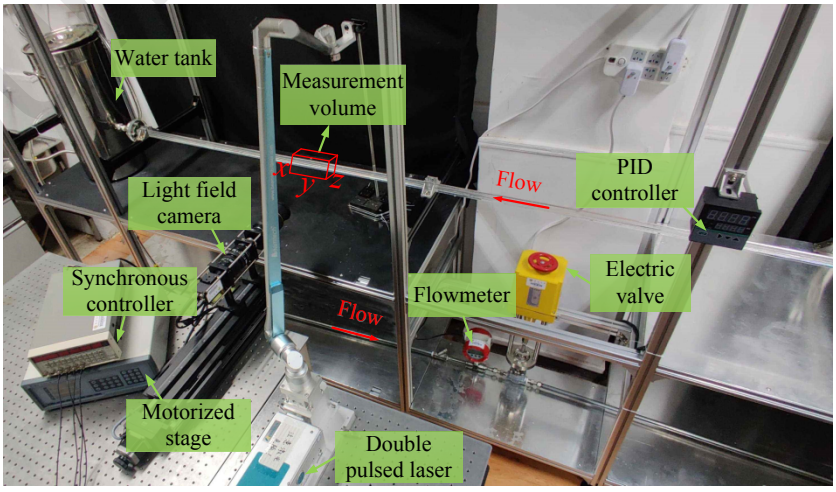

Fig. 14 Experimental setup of the low-speed laminar flow.

For the particle reconstructions, the measurement area is discretized as the 0.1 mm×0.1 mm×0.1 mm voxels and their weight coefficients are calculated by the ERT and DLFC methods, respectively. For the DLFC method, the customized smart calibration board is inserted into the flow from the top of the channel, and the volumetric calibration is carried out for the weight coefficient calculation. The top cover is restored after the calibration to ensure the channel is sealed. In contrast, the calibration of the ERT method is much simpler. The LF camera is initially focused on a smart calibration board stuck on the front wall of the channel, and then moved towards the channel with a distance (d_m) of

$$d_m = t_b + t_w / n_{ag} + 0.5D / n_w \tag{21}$$

where t_w and t_b denote the thickness of the channel wall and calibration board, respectively. In this way, the focal plane of the LF camera can be aligned with the central depth plane of the channel via a single snapshot of the calibration board instead of repeatedly moving it within the measurement area. With the particle volumes reconstructed by SART, the 3D cross-correlation analysis [35] is subsequently performed to yield the velocity field. In this study, using the interrogation volume size of 16×16×16 voxels with an overlap of 50%, the cross-correlation analysis returns 12×16×12 velocity vectors. The spatial resolution of each vector is 1.6 mm×1.6 mm×1.6 mm.

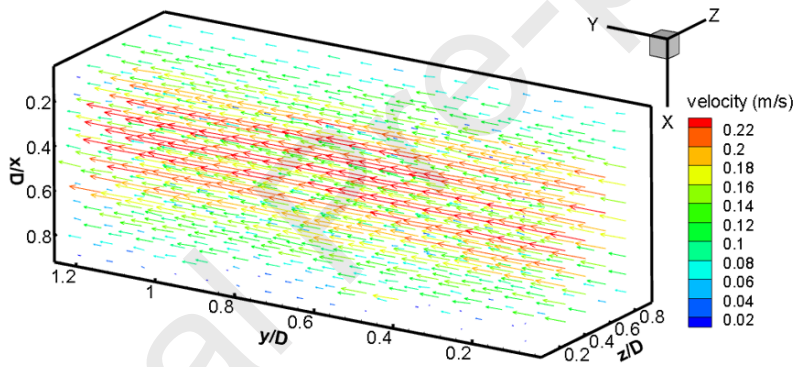

(a) 3D velocity distribution

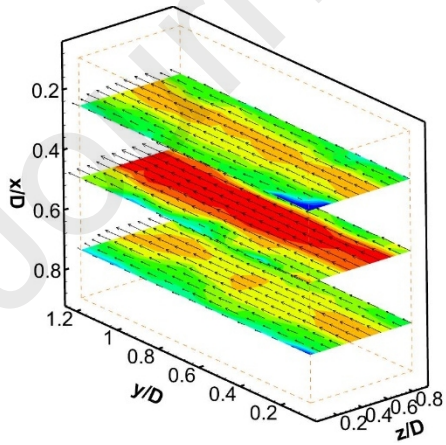

(b) 2D velocity distribution at *y*-*z* slices

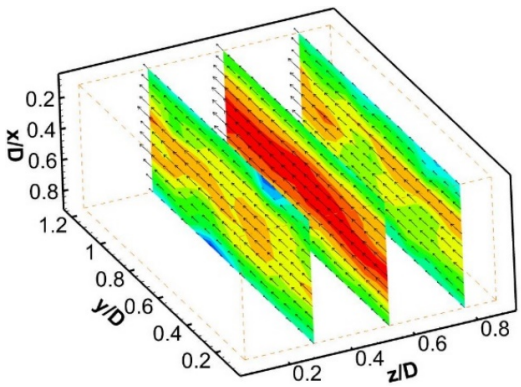

(c) 2D velocity distribution at *x*-*y* slices

Reconstructed velocity distribution by the ERT-SART

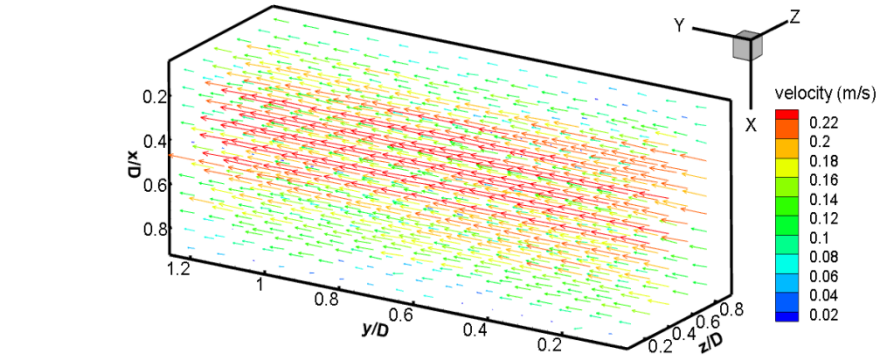

(d) 3D velocity distribution

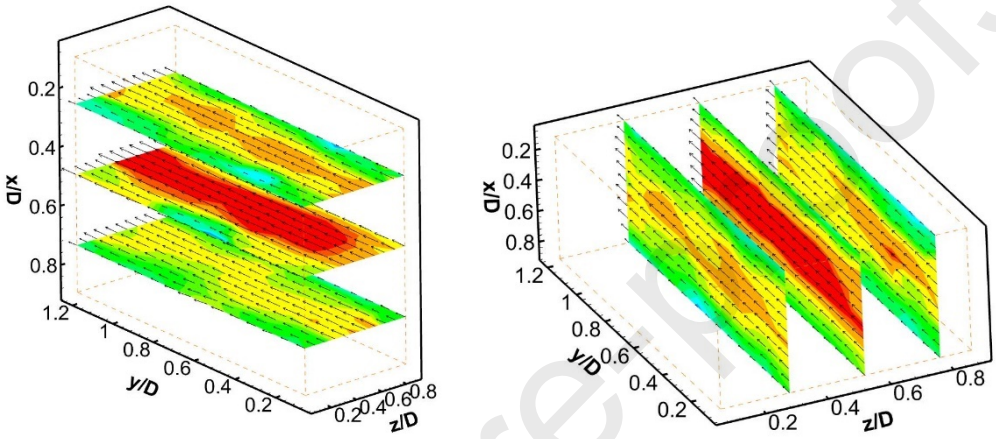

(e) 2D velocity distribution at *y*-*z* slices (f) 2D velocity distribution at *x*-*y* slices

Reconstructed velocity distribution by the DLFC-SART

Fig. 15 Instantaneous laminar flow field reconstructed by ERT-SART and DLFC-SART methods. Note that *y*-*z* slices are taken at $x = 0.24D$, $0.48D$ and $0.72D$, respectively. *x*-*y* slices are taken at $z = 0.3D$, $0.54D$ and $0.78D$, respectively. The contour shows the magnitude of the reconstructed velocity. The size factors of the *x*, *y* and *z*-axis are set to 1:2:1, 1:2:2, 2:2:1 in the 3D plot, *x*-*y* slices plot and *y*-*z* slices plot for a better demonstration.

Figure 15 illustrates an example of the 3D instantaneous velocity field reconstructed by the ERT-SART and DLFC-SART methods. It can be observed that the main flow along the *y*-direction has been successfully reconstructed with the large velocity vectors distributed in the center of the channel. The 2D slices (Figs. 15 (b), (c), (e), (f)) indicate that the velocity magnitude gradually decreases from the center to the wall in both *x* and *z*-directions. The overall velocity distribution is followed the Newtonian fluid flow characteristics in a horizontal channel. The velocity is reduced around the channel wall due to the viscosity of the fluid. The mean velocity reconstructed by DLFC-SART and ERT-SART methods is 0.1150 m/s and 0.1009 m/s, respectively, with a relative error of 6.25% and 6.77%.

To investigate further, a comparative study of the measured velocity with the theoretical calculations is carried out. The theoretical velocity distribution is acquired by computational fluid dynamics (CFD) simulations, where the channel dimensions and Reynolds number are set as the experiment. As the low-speed laminar flow is steady in the fully developed region, the CFD simulation can provide results very close to the ground truth and hence be considered as the theoretical. Fig. 16 illustrates the velocity distributions along *x*-axis at $z/D = 0.3$, 0.54, 0.78 and

along z-axis at x/D = 0.24, 0.48, 0.72, which are extracted from the 3D velocity data. The velocity distributions measured by ERT-SART and DLFC-SART methods are consistent with the theoretical calculation and show an approximately parabolic profile along the x-axis, as illustrated in Fig. 16 (a). The x-y slice closer to the central depth of the channel (z/D = 0.54) has a larger peak velocity. A similar result is also demonstrated on the y-z slices (Fig. 16 (b)) and indicates that both the DLFC and ERT methods are capable of revealing the characteristics of the flow field. However, some discrepancies can be seen between the theoretical and experimental results. For instance, the central high-speed zone is expanded and the velocity gradient gets insignificant (red boxes in Fig. 16 (b)). This is due to the noise contribution of the particle depth elongations to the cross-correlation analysis, which decreases the accuracy of the particle motion estimation. Furthermore, it can be seen from Fig. 16 (a) that the velocity magnitude measured by DLFC and ERT methods at $x/D > 0.8$ is smaller than the theoretical result. This is caused by the motionless bubbles attached to the channel wall in the experiments (illustrated in Fig. 17), which prevents the reconstruction of the tracer particles in that region.

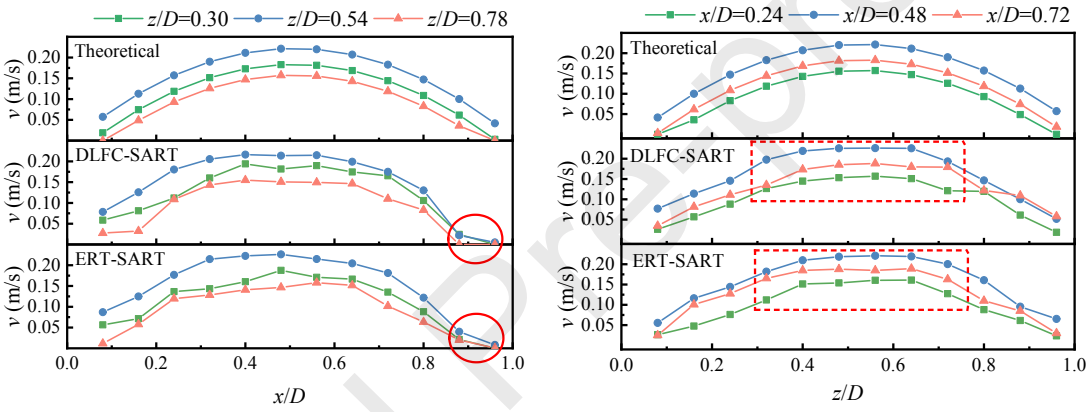

(a) Velocity distribution on x-y slices (b) Velocity distribution on y-z slices

Fig. 16 Velocity distribution at different x-y and y-z slices. (a) x-y slices at z/D = 0.3, 0.54, 0.78. (b) y-z slices at x/D = 0.24, 0.48, 0.72.

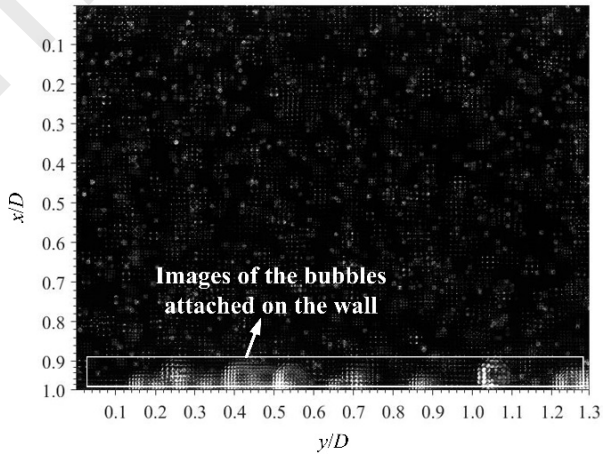

Fig. 17 Experimental light field images of the laminar flow with bubbles attached on the channel wall.

The errors of mean velocity measurement at different x-y and y-z slices are quantitatively evaluated and summarized in Table 4. It can be seen that the velocity error on the y-z slices is more

significant than that on the *x*-*y* slices. This can be interpreted that the particle elongation effect is only demonstrated along the *z*-direction and significantly decreases the measurement accuracy. Therefore, in the LF-PIV, the measurement uncertainty in the depth direction is much higher than that in the lateral direction. Fig. 18 illustrates the cumulative distribution function (CDF) of the velocity measurement error in the whole measurement area. The result indicates that the two methods provide similar measurement accuracy, i.e., more than 75% of measured velocity vectors have a relative error of less than 25%. The feasibility of the proposed ERT method in calculating the weight coefficients of LF-PIV is therefore validated.

Table 4: Mean velocity errors at different *x*-*y* and *y*-*z* slices

	x-*y* slices			*y*-*z* slices		
	$z/D = 0.3$	$z/D = 0.54$	$z/D = 0.78$	$x/D = 0.24$	$x/D = 0.48$	$x/D = 0.72$
DLFC-	4.35%	4.46%	0.13%	7.28%	2.06%	12.01%
ERT-SART	3.51%	1.42%	0.73%	10.43%	4.00%	12.37%

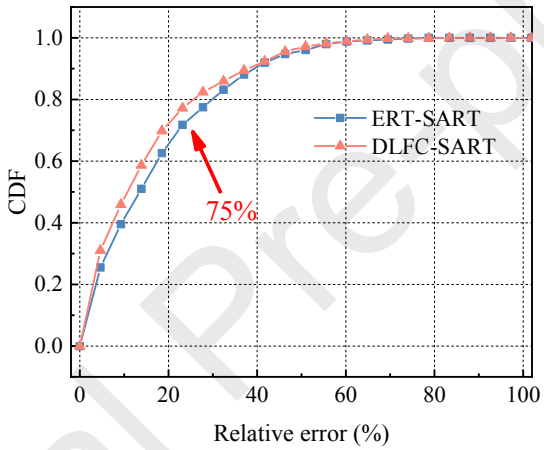

Fig. 18 Cumulative distribution function (CDF) of the velocity measurement errors obtained by ERT-SART and DLFC-SART methods.

5. Conclusions

In this study, an equivalent ray tracing (ERT) method is proposed to calculate the weight coefficients of the light field PIV for accurate particle reconstruction and hence 3D flow measurement. The weight coefficients are calculated through the ray tracing method. The starting points of ray tracing are moved from the sampling points in the target voxels to their equivalent points in the air. To evaluate the feasibility of the proposed method, the calculated weight coefficients were used to reconstruct the spatial locations of the calibration board immersed in the water. Experiments on a low-speed laminar flow were also carried out and the calculated weight coefficients were considered to reconstruct 3D flow velocity. The measurement accuracy was quantitatively evaluated. The concluding remarks achieved from this study are summarized as follows:

- It has been demonstrated that the ERT method can calculate the weight coefficients accurately without prior knowledge of the distances from the flow interfaces to the camera. In practice, they are difficult to measure.

- The ERT method provides a similar accuracy with the in-situ calibration approaches for the 3D target reconstruction and laminar flow measurement. It is suggested that the spatial locations of the calibration board marks can be reconstructed with a mean lateral and depth error of 0.63% and 5.6%, respectively. The overall error of 6.77% is achieved for the velocity measurement.
- Compared with the existing in-situ calibration approaches, the ERT method only requires a single snapshot of the calibration target instead of a series of recordings in the measurement area. With the advantage of simplicity, the ERT method can be used in the LF-PIV for 3D flow measurements in space-constraint applications.

In future, efforts will be made to generalize this method for more challenging conditions such as turbulent flows with curved or arbitrarily shaped windows.

Declaration of Competing Interest

The authors declare that they have no known competing financial interests or personal relationships that could have appeared to influence the work reported in this paper.

References

[1] F. Pereira, M. Gharib, D. Dabiri, D. Modarress, Defocusing digital particle image velocimetry: A 3-component 3-dimensional DPIV measurement technique. Application to bubbly flows, in: Exp. Fluids, 2000. https://doi.org/10.1007/s003480070010.

[2] S. Burgmann, C. Brücker, W. Schröder, Scanning PIV measurements of a laminar separation bubble, in: Exp. Fluids, 2006: pp. 319–326. https://doi.org/10.1007/s00348-006-0153-6.

[3] C.E. Willert, M. Gharib, Digital particle image velocimetry, Exp. Fluids. 10 (1991) 181–193. https://doi.org/10.1007/BF00190388.

[4] J. Katz, J. Sheng, Applications of holography in fluid mechanics and particle dynamics, Annu. Rev. Fluid Mech. 42 (2010) 531–555. https://doi.org/10.1146/annurev-fluid-121108-145508.

[5] D.Y. Wang, H.H. Zhu, B.J. Wang, B. Shi, Performance evaluation of buried pipe under loading using fiber Bragg grating and particle image velocimetry techniques, Measurement. 186 (2021) 110086. https://doi.org/10.1016/j.measurement.2021.110086.

[6] G.E. Elsinga, F. Scarano, B. Wieneke, B.W. Van Oudheusden, Tomographic particle image velocimetry, Exp. Fluids. 41 (2006) 933–947. https://doi.org/10.1007/s00348-006-0212-z.

[7] J. Belden, T.T. Truscott, M.C. Axiak, A.H. Techet, Three-dimensional synthetic aperture particle image velocimetry, Meas. Sci. Technol. 21 (2010). https://doi.org/10.1088/0957-0233/21/12/125403.

[8] T.W. Fahringer, K.P. Lynch, B.S. Thurow, Volumetric particle image velocimetry with a single plenoptic camera, Meas. Sci. Technol. 26 (2015). https://doi.org/10.1088/0957-0233/26/11/115201.

[9] S. Shi, J. Ding, T.H. New, J. Soria, Light-field camera-based 3D volumetric particle image velocimetry with dense ray tracing reconstruction technique, Exp. Fluids. 58 (2017) 78. https://doi.org/10.1007/s00348-017-2365-3.

[10] L. Cao, B. Zhang, J. Li, X. Song, Z. Tang, C. Xu, Characteristics of tomographic reconstruction of light-field Tomo-PIV, Opt. Commun. 442 (2019) 132–147. https://doi.org/10.1016/j.optcom.2019.03.026.

[11] X. Song, M. Gu, L. Cao, Z. Tang, C. Xu, A microparticle image velocimetry based on light field imaging, IEEE Sens. J. 19 (2019) 9806–9817. https://doi.org/10.1109/JSEN.2019.2927414.

[12] Y. Ji, J. Wu, Calibration method of light-field camera for photogrammetry application, Measurement. 148 (2019) 106943. https://doi.org/10.1016/j.measurement.2019.106943.

[13] J. Sun, C. Xu, B. Zhang, M.M. Hossain, S. Wang, H. Qi, H. Tan, Three-dimensional temperature field measurement of flame using a single light field camera, Opt. Express. 24 (2016) 1118. https://doi.org/10.1364/oe.24.001118.

[14] R. Ng, Digital light field photography, Stanford Univ. (2006) 1–203. https://www.lytro.com/renng-thesis.pdf%5Cnhttp://testcis.cis.rit.edu/~cnspci/references/dip/light_field_photography/ng2006.pdf.

[15] T.W. Fahringer, B.S. Thurow, Plenoptic particle image velocimetry with multiple plenoptic cameras, Meas. Sci. Technol. 29 (2018). https://doi.org/10.1088/1361-6501/aabe1d.

[16] G.T. Herman, A. Lent, Iterative reconstruction algorithms, Comput. Biol. Med. 6 (1976) 273–294. https://doi.org/10.1016/0010-4825(76)90066-4.

[17] Reference details omitted for double-anonymized reviewing.

[18] S. Shi, J. Wang, J. Ding, Z. Zhao, T.H. New, Parametric study on light field volumetric particle image velocimetry, Flow Meas. Instrum. 49 (2016) 70–88. https://doi.org/10.1016/j.flowmeasinst.2016.05.006.

[19] J. Sun, H. Wang, X. Zhu, A fast underwater calibration method based on vanishing point optimization of two orthogonal parallel lines, Measurement. 178 (2021) 109305. https://doi.org/10.1016/j.measurement.2021.109305.

[20] S.M. Soloff, R.J. Adrian, Z.C. Liu, Distortion compensation for generalized stereoscopic particle image velocimetry, Meas. Sci. Technol. 8 (1997) 1441–1454. https://doi.org/10.1088/0957-0233/8/12/008.

[21] B. Wieneke, Volume self-calibration for 3D particle image velocimetry, Exp. Fluids. 45 (2008) 549–556. https://doi.org/10.1007/s00348-008-0521-5.

[22] B. Wieneke, Improvements for volume self-calibration, Meas. Sci. Technol. 29 (2018) 084002 (15pp). https://doi.org/10.1088/1361-6501/aacd45.

[23] C. Gray, B. Wieneke, Volume self-calibration for stereo-PIV and tomographic-PIV, in: 9th Int. Symp. Fluid Control Meas. Vis. 2007, FLUCOME 2007, 2007.

[24] J. Soria, C. Atkinson, Towards 3C-3D digital holographic fluid velocity vector field measurement - Tomographic digital holographic PIV (Tomo-HPIV), Meas. Sci. Technol. 19 (2008). https://doi.org/10.1088/0957-0233/19/7/074002.

[25] F. Scarano, Tomographic PIV: Principles and practice, Meas. Sci. Technol. 24 (2013) 012001. https://doi.org/10.1088/0957-0233/24/1/012001.

[26] R. Ben Salah, O. Alata, L. Thomas, B. Tremblais, L. David, 3D particle volume tomographic reconstruction based on marked point process: Application to Tomo-PIV in fluid mechanics, in: ICASSP, IEEE Int. Conf. Acoust. Speech Signal Process. - Proc., 2014: pp. 8153–8157. https://doi.org/10.1109/ICASSP.2014.6855190.

[27] E.M. Hall, T.W. Fahringer, D.R. Guildenbecher, B.S. Thurow, Volumetric calibration of a plenoptic camera, Appl. Opt. 57 (2018) 914. https://doi.org/10.1364/ao.57.000914.

[28] S. Shi, J. Ding, T.H. New, Y. Liu, H. Zhang, Volumetric calibration enhancements for single-camera light-field PIV, Exp. Fluids. 60 (2019) 21. https://doi.org/10.1007/s00348-018-2670-5.

[29] T. Georgiev, C. Intwala, Light field camera design for integral view photography, Adobe Syst. Inc. Tech. Rep. (2003) 1–13. http://citeseerx.ist.psu.edu/viewdoc/download?doi=10.1.1.104.213&rep=rep1&type=pdf.

[30] Reference details omitted for double-anonymized reviewing.

[31] Z. Wang, A.C. Bovik, H.R. Sheikh, E.P. Simoncelli, Image quality assessment: From error visibility to structural similarity, IEEE Trans. Image Process. 13 (2004) 600–612.

https://doi.org/10.1109/TIP.2003.819861.

[32] L. Thomas, B. Tremblais, L. David, Optimization of the volume reconstruction for classical Tomo-PIV algorithms (MART, BIMART and SMART): Synthetic and experimental studies, Meas. Sci. Technol. 25 (2014). https://doi.org/10.1088/0957-0233/25/3/035303.

[33] E.A. Deem, Y. Zhang, L.N. Cattafesta, T.W. Fahringer, B.S. Thurow, On the resolution of plenoptic PIV, Meas. Sci. Technol. 27 (2016) 084003. https://doi.org/10.1088/0957-0233/27/8/084003.

[34] S. Shi, J. Ding, C. Atkinson, J. Soria, T.H. New, A detailed comparison of single-camera light-field piv and tomographic piv, Exp. Fluids. 59 (2018) 1–13. https://doi.org/10.1007/s00348-018-2500-9.

[35] F. Scarano, M.L. Riethmuller, Advances in iterative multigrid PIV image processing, Exp. Fluids. 29 (2000) S051–S060. https://doi.org/10.1007/s003480070007.

- A novel ray-tracing method (ERT) is proposed for calculating weight coefficients of light field PIV.
- The basic principle, derivation and implementation of the ERT method are described.
- Numerical reconstruction and experimental measurements on a laminar flow are conducted to evaluate the proposed method.
- The performance of the ERT method is compared with the in-situ calibration method.
- The potential applications of the ERT method as well as the challenging problems are outlined.

CRediT authorship contribution statement

Xiaoyu Zhu: Conceptualization, Methodology, Data curation, Writing - original draft. **Md. Moinul Hossain:** Technical discussion, Writing - review & editing. **Jian Li:** Visualization, Funding acquisition. **Biao Zhang:** Software. **Chuanlong Xu:** Supervision, Project administration, Funding acquisition.